Low-Dimensional Perovskite Nanoplatelet Synthesis Using *in situ* Photophysical Monitoring to Establish Controlled Growth

Mai Do,† Irene Kim, ‡++ Matthew A. Kolaczkowski,++† Jun Kang,+ Gaurav Kamat,++ Zhenghao Yuan,‡ Nicola S. Barchi,‡# Lin-Wang Wang,+ Yi Liu,†+ Matthew J. Jurow,†+* Carolin M. Sutter-Fella‡**

† The Molecular Foundry, Lawrence Berkeley National Laboratory, Berkeley, CA 94720, United States

‡ Chemical Sciences Division, Lawrence Berkeley National Laboratory, Berkeley, California 94720, United States

+ Materials Sciences Division, Lawrence Berkeley National Laboratory, Berkeley, California 94720, United States

++ College of Chemistry, University of California, Berkeley, Berkeley, California 94720, United States

Laboratory of Semiconductor Materials, Ecole Polytechnique Fédérale de Lausanne, CH-1015 Lausanne, Switzerland

Perovskite nanoparticles have attracted the attention of research groups around the world for their impressive photophysical properties, facile synthesis and versatile surface chemistry. Here, we report a synthetic route that takes advantage of a suite of soluble precursors to generate $CsPbBr_3$ perovskite nanoplates with fine control over size, thickness and optical properties. We demonstrate near unit cell precision, creating well characterized materials with sharp, narrow emission lines at 430, 460 and 490 nm corresponding to nanoplates that are 2, 4, and 6 unit cells thick, respectively. Nanoplates were characterized with optical spectroscopy, atomic force microscopy, scanning electron microscopy and transmission electron microscopy to explicitly correlate growth conditions, thickness and resulting photophysical properties. *Detailed in situ* photoluminescence spectroscopic studies were carried out to understand and optimize particle growth by correlating light emission with nanoplate growth across a range of synthetic conditions . It was found that nanoplate thickness and emission wavelength increase as the ratio of oleic acid to oleyl amine or the reaction temperature is increased. The temperature and ligand-dependent growth process environment reveal a growth process governed by both thermodynamic and kinetic factors. Using this information, we control the lateral size, width and corresponding emission wavelength of the desired nanoplates by modulating the temperature and ratios of ligand.

Introduction

Two-dimensional nanomaterials have attracted considerable research attention for fundamental scientific and technological applications due to their large specific surface area, controllable quantum confinement, orientable assemblies, and exciting physical and optoelectronic properties.[1-5] The recent synthesis and isolation of materials like graphene, and two-dimensional nanostructures of transition metal carbides or nitrides (MXenes), metal alloys and semiconductors have considerably expanded the family of two-dimensional nanomaterials.[1, 2, 6-12] The development of quasi two-dimensional lead halide perovskite nanoplates has added these versatile fluorophores to the list of functional two-dimensional nanomaterials.[1, 2, 12]

Lead halide perovskites have the formula of $APbX_3$ where A is a monovalent cation, usually Cs^+, $CH_3NH_3^+$ (MA), or $CH(NH_2)_2^+$ (FA), and X is a halide (Cl^-, I^-, Br^-). The general cubic perovskite crystal structure is a common corner sharing octahedral.[1,14] The family is divided into two broad groups: organic-inorganic hybrid type lead halide perovskites and all-inorganic lead halide perovskites.[13] Research involving perovskite nanoparticles has been recently driven forward by the initial report of a colloidal synthesis by hot injection.[14] This simple synthesis yields particles with band gap energies tunable between 410-700 nm, narrow emission lines and PLQY values above 85%.[2, 7, 12, 14] Continued work has yielded synthetic pathways that offer control over particle size that can be varied across the Bohr exciton radius of 7 nm, resulting in particles with customizable degrees of exciton confinement.[4, 15] A subsequent adaptation of the initial colloidal synthesis at lower temperature resulted in the production of thin $CsPbX_3$ platelets with photoluminescence peaks tunable between 385 nm and the emission of the bulk, 520 nm for $CsPbBr_3$.[2] $CsPbX_3$ is thus one of the latest entrants into the field of ultrathin semiconducting nanoparticles.[1] Several other synthetic routes to perovskite nanostructures, including platelets, have recently been reported which control particle size and shape offered through control of reaction temperature and ligand choice.[12, 16-19] Perovskite's tunable form factor coupled with their unique photophysical properties introduced by two-dimensional confinement promise to expand applications in efficient solar cells, bright light-emitting diodes, sensors and other photonic devices.[20-24] Here, we focus on the synthesis and characterization of nanoplatelets as they exhibit a large aspect ratio which creates anisotropic properties that are highly valued in optoelectronics,[30]biological systems and energy storage.[25-27,28, 29]

Despite burgeoning research in this field, $CsPbBr_3$ nanoparticles are difficult to reliably synthesize and especially purify. A careful analysis of the mechanism of particle formation and the synthetic components needed to control particle growth is necessary to satisfy the need for a robust and reproducible synthesis of two-dimensional nanoparticles. In this report, we have modified a synthetic methodology based on a benzoyl bromide precursor, originally developed to generate $CsPbBr_3$ nanocubes that are attainable at 170 °C with photoluminescence (PL) emission at 512 nm, to create monodisperse $CsPbBr_3$ nanoplatelets with tunable thicknesses and sizes by lowering the reaction temperature to 60–100 °C.[18] These low temperatures enabled both shape and thickness control, leading to emission in the not well covered blue

region of the spectrum. We prepared $CsPbBr_3$ nanoplates with controlled thicknesses and sharp, narrow emission lines at 430, 460, and 490 nm. In addition to traditional electron microscopy, atomic force microscopy, and photophysical analysis, we employ *in situ* PL spectroscopic studies to track light emission of the growing nanoplates during the reaction as a function of temperature and ligand environment. *In situ* PL has been used previously as a revealing tool to monitor nanocrystal synthesis. [1, 14, 16] It was found that the PL emission peak red shifts and narrows over time, corresponding to nanoparticle nucleation and growth.[1] Additionally, Dong et al. showed that the terminal PL wavelength during synthesis stabilizes at high Br/Pb ratio or continues to steadily increase at low Br/Pb ratio.[16] A continuous increase in PL intensity over time was attributed to an increase in the number of quantum dots.[16]

In the present work, we systematically correlate synthesis conditions to PL emission wavelength by monitoring nanoparticle growth over the full course of the reaction, and find that growth of $CsPbBr_3$ nanoplates (using the below described chemistry) is governed by both a thermodynamic factor, mediated by the ligands introduced in the reaction, and a kinetic factor, depending on the reaction temperature. In total, thinner nanoplates with more strongly confined excitons and higher emission energy (shorter emission wavelengths) can be isolated by decreasing temperature or decreasing the ratio of oleic acid to oleylamine.

Results and Discussion

Synthesis

The first report of $CsPbBr_3$ nanoplates[2] used an adapted synthetic route from the colloidal synthesis of $CsPbBr_3$ nanocubes[14] where the reaction temperature was lowered during particle growth to 90 – 130 °C. In both of these procedures, for either cubes or plates, cesium oleate is prepared from cesium carbonate and oleic acid, and separately, lead bromide is dissolved in octadecene with oleic acid (OA) and oleylamine (OLAm). The two solutions are heated independently and mixed briefly before quenching in an ice bath. This technique is effective, but produces platelets with low yield and with a distribution of thicknesses. To our knowledge, the thinnest $CsPbBr_3$ nanoplates synthesized from this procedure have a thickness of 3.0 $\pm$0.4 nm that is comparable to 5 unit cells of perovskite.[1] As a result, we have selected and followed a different synthetic procedure to produce thinner nanoplates composed of a smaller number of unit cells with emission as low as 430 nm. To improve purity and dimensional control, we have adapted a synthetic route that uses a benzoyl bromide precursor in place of lead halide to generate monodisperse particles with tunable thicknesses. This procedure is rooted in chemistry initially developed to create monodisperse nanocubes.[18] By then controlling the mixture of alkyl ligands and the reaction temperature, a reliable procedure to synthesize size-tunable $CsPbBr_3$ nanoplates is demonstrated.

In a typical reaction, lead acetate trihydrate and cesium carbonate is first suspended in octadecene. To this mixture, dry oleic acid and oleyl amine are added. After the temperature is lowered to the required

value (see experimental methods for details), benzoyl bromide is quickly added, and the reaction mixture immediately cooled down in an ice-water bath. Since the halide-precursor is injected directly into the cation-precursor solution at a designated temperature, the synthesis avoids forming a poorly soluble oleylammonium halide salt before generating nanoparticles.[1, 14] The elevated temperature required to keep these species soluble in other preparation methods makes the production and isolation of thin nanoplates difficult or impossible. Consequently, the procedure introduced here uses significantly lower temperatures ranging from 60 – 100 °C while others used 90 – 130 °C,[2] 150 °C,[1] or 80 – 180 °C [31] to obtain $CsPbBr_3$ nanoplates.

To purify the platelets, the crude reaction mixture is centrifuged and the pellet dispersed in toluene. Toluene is preferred to hexane at this stage because of the higher polarity index (2.4 relative to hexane's 0.1), which avoids forming a colloid resistant to further purification.[32] Ethyl acetate was selected as an anti-solvent to precipitate the particles because of its limited polarity index (4.4), ensuring that the labile surface ligands are preserved.[33] Higher polarity solvents can strip surface ligands, leading to sintering and reconstruction of nanoplates and the formation of bigger particles with redshifted emission. Critically, the nanoplates must fully disperse in the solvent before the addition of the anti-solvent to prevent aggregation. The mixture of nanoplates, solvent and anti-solvent is then centrifuged to isolate the clean $CsPbBr_3$ platelets. This cycle of precipitation is repeated two more times before the nanoplates are dispersed in either toluene or hexanes for further use. The thinnest nanoplates, emitting at 430 nm, are only stable in hexanes.

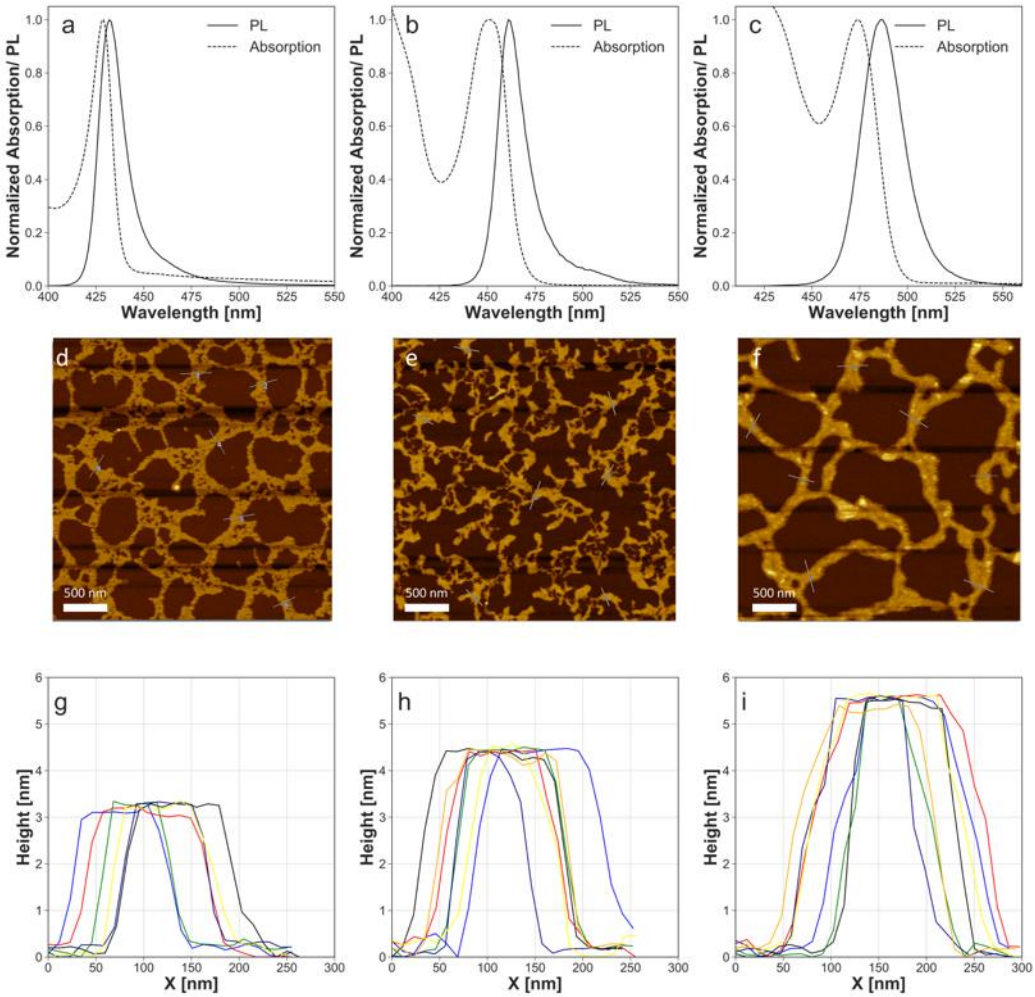

Figure 1. UV absorption and PL spectra of (a) 2 unit cell, (b) 4 unit cell and (c) 6 unit cell thick $CsPbBr_3$ nanoplates showing quantum size effects. AFM topography images of $CsPbBr_3$ nanoplates (d) 2 unit cells, (e) 4 unit cells and (f) 6 unit cells thick. The white lines show the scans for the thickness profile plotted below. Line profiles indicate the thickness of particles to be (g) 2 unit cells, (h) 4 unit cells and (i) 6 unit cells.

UV-Vis absorption spectra, photoluminescence and atomic force microscopy

In general, purified particles demonstrate a small Stokes shift (compare Figures 1 a-c) common to perovskite nanoparticles, associated with a direct exciton recombination process.[7] Samples of thicker nanoplates show a redshift of both UV absorption and PL emission peaks. The Stokes shift also increases, from 3 to 13 nm as particles grow from 430 nm emitters to 490 nm emitters. The narrow full width at half maximum (FWHM) values of the emission at room temperature are indicative of the narrow size dispersions of the isolated platelets. All isolated nanoplates have an x-ray diffraction pattern that overlaps with the calculated reflections from an ideal cubic $CsPbBr_3$ perovskite crystal (Figure S1).

Next, we use atomic force microscopy (AFM) to examine the nanoplate thickness. AFM has been used previously to extract the thickness of $CH_3NH_3PbI_3$ NPLs, from which a2 nm thickness was assigned to 3 unit cells.[34] The AFM results are shown in Figures 1 d-f. The average height measured by AFM is the sum of the nanoplates thicknesses combined with two layers of organic surface ligands (see methods), each estimated to contribute 1 nm of thickness to the measured value.[35] A cubic $CsPbBr_3$ perovskite unit cell is a corner sharing octahedron with 6 Å edges.[36] Adjusting for the thickness of the ligands, 4-unit cell thick (2.4 nm) $CsPbBr_3$ nanoplates emit light at 460 nm. The 2-unit cell thick and 6-unit cell thick nanoplates emit light at 430 nm and 490 nm and have an average ligand-free thickness of 1.2 and 3.5 nm, respectively. Analysis of the AFM images confirms that the height (thickness) of the nanoplates increases with increasing PL emission wavelength, suggesting a correlation between PL emissions with nanoplate thickness. In a previous report, high resolution TEM was used to associate emission at 2.70 eV (459 nm) with 5, 2.76 eV (449 nm) with 4, and 2.83 eV (438 nm) with 3 monolayers, respectively.[1] This slight variation of our results compared to the literature might be related to the use of different characterization methods, where high resolution TEM directly probes the nanoplatelets, we used a thin film of polymerized methane to prevent aggregation of the AFM samples. A comparison of literature results of emission wavelength versus unit cell thickness is illustrated in Figure 2 and clearly highlights some fluctuations within results from different groups.

Density functional theory calculation

To understand the impact of particle size in unit cell layers on the resulting photoluminescence emission wavelength, the band gap of 1-6 unit cell thick $CsPbBr_3$ nanoplates with infinite lateral dimensions was calculated from density functional theory (DFT) and compared with experimental results (Figure 2). DFT has a tendency to underestimate the band gap in some particles, but usually yields appropriate differences between the band gaps of nanostructures relative to the bulk (ΔE_g, the quantum size effect induced blue shift, Figure S2).[37] The measured values correspond relatively well with the calculated band gaps despite the discrepancy caused by the assumption of an infinite aspect ratio in the model.

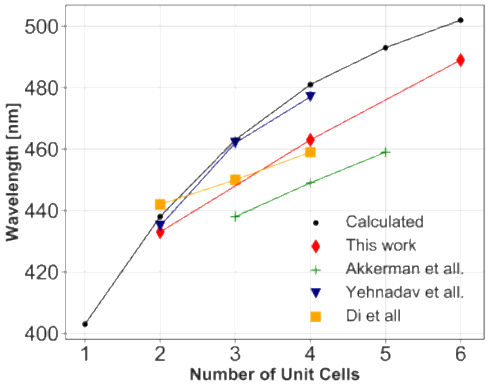

Figure 2. Calculated and experimental values of the emission wavelength of $CsPbBr_3$ perovskite nanoplates with thickness specified in unit cells. Reference data for comparison taken from […].

Electron microscopy characterization

Platelets were also characterized with TEM (Figure S3) and SEM (Figure S4). The approximate average edge length of are 50, 30 and 20 nm for 4, 5, and 6 unit cell thick rectangular or square nanoplates, respectively, indicating that the levers that control particle thickness also affect the particle size in the other two dimensions (Figure 3). It is noted that nanoplates with thicknesses < 4 unit cells could not be characterized by TEM because of rapid damage in the electron beam.

Figure 3. TEM size distribution histograms of (a) 4 unit cell, (b) 5 unit cell and (c) 6 unit cell $CsPbBr_3$ nanoplates.

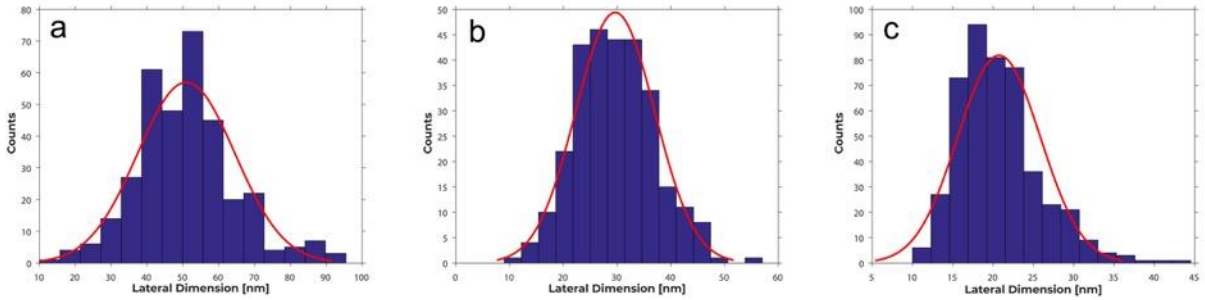

Analysis of particle growth from in situ PL measurements

The evolution of the emission wavelength of $CsPbBr_3$ nanoplates during formation was studied by a customized *in situ* PL setup as illustrated in Figure S5. The progression of *in situ* PL spectra during nucleation and growth is plotted in Figure 4a and Figures S6-S20, which shows several features. First, the PL intensity increases quickly during nanoplatelet growth. The absolute intensity depends on the probed quantity and quality of the nanoplatelets as well as potential reflection from the test tube due to minor variation between the incoming laser beam angle and the test tube. Second, the shape of the spectra is changing, starting with a broad emission peak centered around 475 nm stemming from the organic precursors which immediately narrows upon injection of benzoyl bromide within less than 100 ms (see Fig. S21 in SI) due to seed formation and growth. This observation has been made by others as well.[1] Third, a weak PL side peak around 540 nm is observed mostly at higher reaction temperatures. It is likely that at elevated temperature side products with emission around 540 nm form. A very similar side peak (~543 nm) has been observed by Protesescu et al.[14] Finally, the change in the PL signal during particle growth is characterized by two regimes. First, the emission wavelength is red shifting over time once benzoyl bromide is injected to induce seed formation and nanoplatelet growth, similar to what has been described before.[1] Additionally, we interpret this red shift with thickening of the nanoplates based on the correlation of emission

wavelength and thickness as discussed before. The growth mode then is saturated with constant emission wavelength, indicative of a termination of the thickening process. This is supported by the findings of Yang et al. who reported constant NPL thickness and increasing lateral dimensions over time.[31]

To understand and optimize synthetic control of final particle size and especially thickness, we independently varied reaction temperature and ligand ratio (OA:OLAm = 1:1, 1:2, or 1:3) in the reaction mixture, yielding mechanistic insights into the influence of synthetic conditions. Figures 4c-e present the PL emission wavelength over time. As the temperature is raised from 60 °C to 100 °C for OA:OLAm = 1:3 emission increases from … nm to … nm. When comparing the PL evolution of different ligand ratios at the same temperature, the final PL emission wavelength is larger for reaction mixtures richer in oleic acid, e.g. 479 nm for OA:OLAm = 1:3 and 489 nm for OA:OLAm = 1:1 at 60°C (Figure 4c). On the basis of the correlation between PL emission wavelength and nanoplate thickness, we find that final particle thickness depends on both the ratio of OA:OLAm and the reaction temperature. No information about overall particle size can be gleaned from this measurement, as increases in lateral size do not impact emission wavelength which is dominated by the quantum confinement effect.

To describe the kinetics of the *in situ* PL data, a horizontal line is drawn which represent the terminal PL emission wavelength. We extracted the terminal wavelength under the different synthetic conditions (ligand ratio and temperature) by two measurements with geometrically different setups (compare Figures S5 and S22) and find not surprisingly that the terminal wavelength is independent of the setup, but the time to reach the terminal wavelength is dominated by the diffusion of the benzoyl bromide in solution. Qualitatively, we conclude that the terminal time is the same at a given reaction temperature but the rate is increased at higher OLAm concentrations. It is worth mentioning that the terminal emission wavelength under the same synthetic conditions is reproducible as shown in Figures 5 and S23.

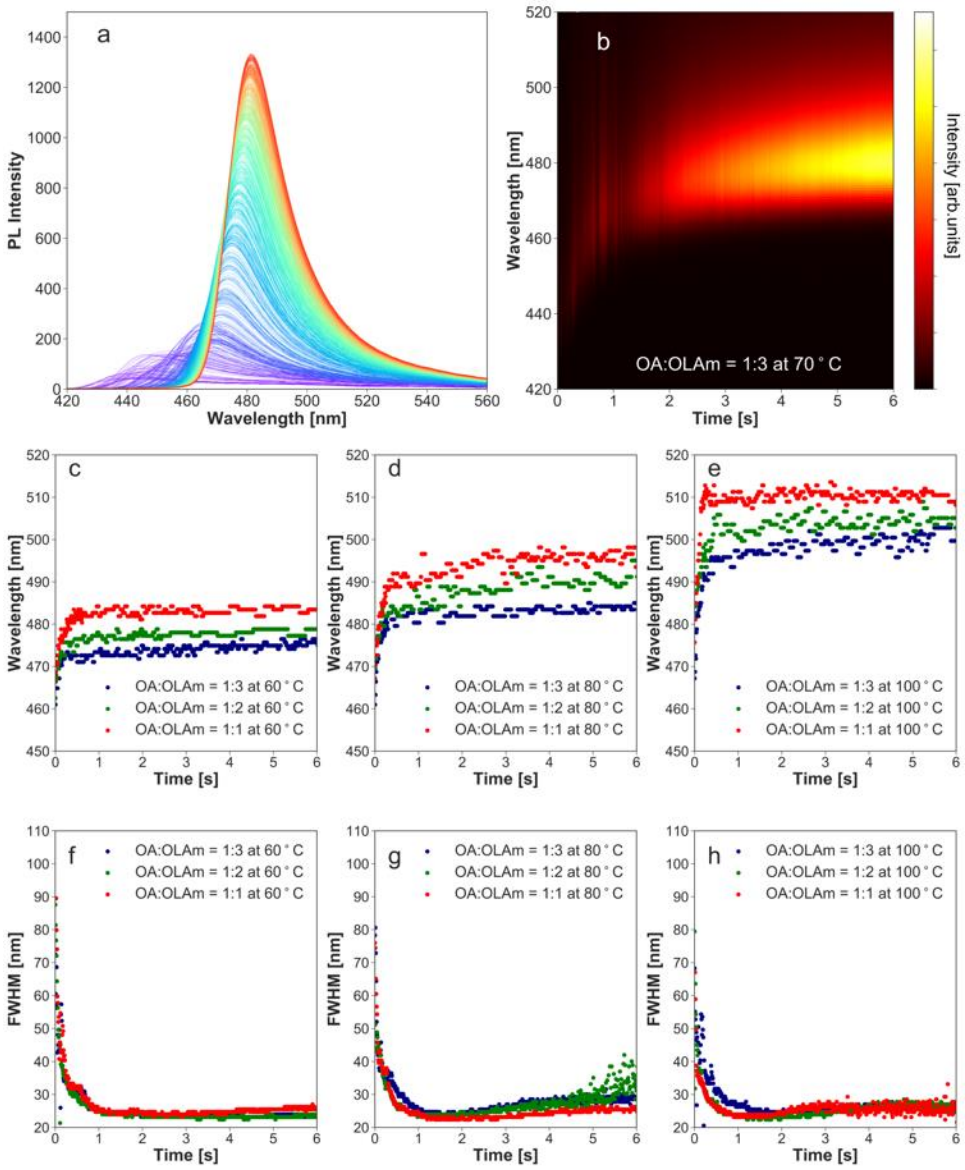

Figure 4. Typical PL spectra and contour plot collected during NPL synthesis (a,b). Evolution of emission wavelength (c-e) and FWHM (f-h) over time extracted from *in situ* PL measurements of nanoplates grown under specified OA:OLAm ratios at 60 °C, 80 °C and 100 °C.

The full width at half maximum value for each PL spectrum is calculated every 10 ms (Figure 4f-h). For all reactions, the PL FWHM decreases steadily until reaching about 25 nm within about one second. Differences in the FWHM values are only visible below 1 s. The FWHM is independent of the ligand ratios used.

To describe and quantify the *in situ* PL data, we fit the evolution of the emission wavelength with two linear fits (one for the fast increase and one for the slow increase). To obtain a good linear fit, thirty data points are used to initiate the regression and more data points (at increasing time) are taken consecutively until the coefficient of determination (r_2) is greater than or equal to 0.85. The coefficient of determination is the square of the correlation coefficient *r,* the Pearson product-moment correlation coefficient.[38] The value of r_2 will be close to 1 when the data closely fits the linear equation. The asymptotic second region consists of many data points with the same peak PL wavelength that can be used to generate a good linear fit. Since there are many data points with similar values in this region, the r_2 value between the first selected data points starting from the final reaction time begins with a relatively high value close to 1. However, this does not accurately describe the second region as it tends to over fit the emission of the particles after growth has terminated (Figure 5). To avoid this error, data points from smaller time values are added until r_2 is less than or equal to 0.85, yielding a more satisfying fit equation. From the intersection of the two linear regressions, we assign an intercept that reflects the transition from growth to termination. The linear fits at the full range of tested temperatures at specified OA:OLAm ratios are displayed in Figure S7 and summarized in table S1.

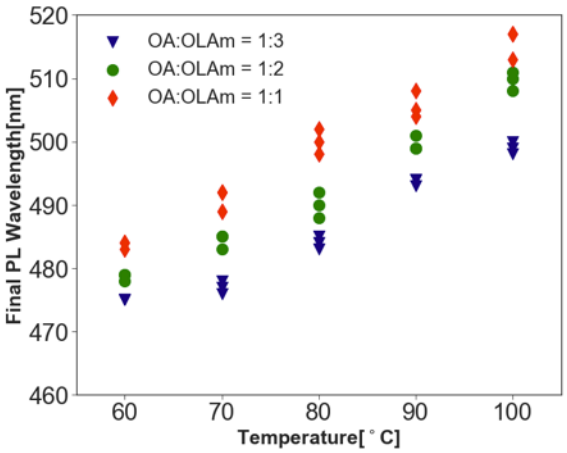

Figure 5. Final emission wavelengths of nanoparticles grown with specified ligand ratios and temperatures extracted from *in situ* PL measurements.

Proposed reaction mechanism

From the *in situ* PL measurements we identify two different regimes, one very short, where the emission wavelength is red shifting, followed by a regime with constant emission wavelength. The thickness of the NPLs related to the red shift is plateaued within less than one second which is controlled by the temperature and ligand ratio. At a specific temperature, ligand mixtures richer in oleic acid generate thicker particles. One growth theory for nanoparticles suggests that the removal of high-energy facets leads to a

decrease in overall surface energy.[39] Capping ligands contribute to the reduction of the overall surface energy and therefore influence the final shape of the nanostructure. Since oleylammonium has more favorable surface binding interactions at lower temperatures, the average thickness of nanoparticles is reduced.[4, 16, 33] We have found that particles made from a 1:3 ratio of ligands are thinnest while a 1:1 ratio of the same ligands generates the thickest plates. This correlation between the thickness of the synthesized nanoplates and the OA:OLAm ratio demonstrates the importance of a contributing thermodynamic component governing particle growth. This is possibly caused by a surface energy relationship in which additional oleylamine favors the production of high aspect ratio particles.

Furthermore, the bonding equilibria between ligands should be considered to examine ligand interactions that may contribute to nanoparticle thickness growth (Figure 6). OLAm is in dynamic equilibrium with its conjugated acid oleylammonium cation ($OLAH^+$) in the presence of OA and its conjugated base oleate anion (OA^-).[4, 33, 39-41] Upon the addition of benzoyl bromide, Br^- is generated from the reaction between OLAm and benzoyl bromide, which servesas the halide source to help form and stabilize NPLS. As supported in other studies, the $OLAH^+$ interacts with Br^- and the OA^- competes with Cs^+ ions to bind to the nanoplates.[4, 41] It is speculated that a greater molar availability of OLAm relative to OA increases the concentration of $OLAH^+$ in the mixture, which couples with the available Br^- ions and slows the growth of nanoplates in the vertical dimension. Due to the stoichiometry between the Cs^+ and Br^- in the $CsPbBr_3$ perovskite structure, the higher ratio of OA to OLAm will slow the growth of the nanoplate thickness.[4, 40]

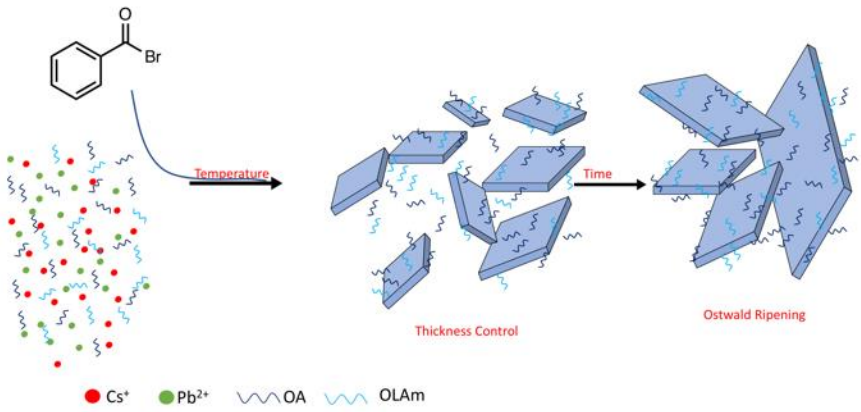

Figure 6. Schematic drawing of the proposed reaction scheme with reaction temperature and ligand ratio as parameters to control thickness while reaction time influences platelet size, similar to the process described by Yang et al..[31]

Conclusions

We have developed a synthetic procedure in which separate lead cation and halide anion precursors are used to generate monodisperse and pure $CsPbBr_3$ perovskite nanoplates of discrete thicknesses. 2-, 4-, and 6-unit cell thick platelets can be synthesized and isolated with sharp, narrow emission lines at 430 nm, 460 nm, and 490 nm, respectively. We make use of the correlation between PL emission wavelength and nanoplate thickness to interpret *in situ* PL results during nanoplatelet synthesis with variation of temperature and ligand ratio (OA:OLAm = 1:1, 1:2, or 1:3). It was found that nanoplate thickness, and emission wavelength of the purified particles, increases as the ratio of oleic acid to oleyl amine or the reaction temperature is increased. By understanding the growth process and carefully analyzing the photoluminescence of the particles during the reaction, particles of specific size and color can be synthesized. It was demonstrated that *in situ* PL spectroscopy is a viable characterization method to track nanoparticle growth. It can be used to optimize synthetic procedures efficiently.

Methods

Materials.

Cesium carbonate (Cs_2CO_3, 99%, Aldrich), lead acetate trihydrate ($Pb(CH_3COO)_2{\cdot}3H_2O$, 99.999%, Aldrich), 1-octadecene (ODE, 90%, Aldrich), benzoyl bromide (C_6H_5COBr, 97%, Aldrich) were used without purification. Oleic acid (OA, 97%, Acros Organic), and oleylamine (OLAm, 70%, Aldrich) were dried in vacuum for an hour before use.

Density Functional Theory Calculations.

DFT calculations were performed using the Vienna ab initio simulation package (VASP).[42] The core−valence interaction is described by the projector-augmented wave (PAW) method.[43] The cutoff for planewave expansion is set to 300 eV. Structures are relaxed until the force on each atom is smaller than 0.01 eV/Å. The generalized gradient approximation of Perdew−Burke−Ernzerhof (GGA-PBE) is adopted,[44] and the spin-orbital coupling (SOC) interaction is also considered. A vacuum layer larger than 14 Å is used to avoid interaction between periodic images. The Brillouin zone is sampled by a Γ-centered 3×3×1 k-point mesh.

In situ Photoluminescence.

The measurement set-up includes a 405 nm laser source that passes through the reaction sample, which is heated to a certain temperature in an aluminum heating block on a hot plate. Following the laser source, there is a laser line filter to reduce the spectral noise. A focus lens (F = 50.0 mm) is placed after the laser line filter. After the reaction sample, a blocking edge long-pass filter (409 nm) is attached to remove scattered light from the excitation source. A second lens (F = 25.4 mm) is placed to focus the light onto the detector unit and relay the information through the optical fiber to the QE *Pro* spectrometer (*Ocean Optics*), which provides intensity and corresponding wavelength data taken every 10 milliseconds in the Oceanview computer software. The schematic of the *in situ* photoluminesence setup is shown in the ESI (Figure S5). The PL emission intensity, normalized PL spectra, and contour plots of each reaction at a specified OA:OLAm ratio and temperature are shown in Figures S8-S22.

Synthesis and Purification of $CsPbBr_3$ Nanoplates.

2 layer thick nanoplates

Cesium carbonate (24.32 mg, 0.074 mmol), lead acetate trihydrate (114 mg, 0.3 mmol) and ODE (7.5 mL, 23.4 mmol) were loaded into a 20 mL vial and dried under vacuum for 1h at 120 °C. To this suspension, dry OA (1.48 ml, 4.5 mmol) and OLAm (0.47 ml, 1.5 mmol) were added under an inert atmosphere, and precursors were allowed to dissolve with stirring for 30 minutes. The temperature was then lowered to 60 °C and allowed to stabilize for 10 minutes. Benzoyl bromide (0.11 mL, 0.9 mmol) was added quickly and the reaction mixture was immediately cooled down in an ice-water bath. The resulting crude product is strongly emissive.

The purification of perovskite nanoparticles is difficult and fickle. The crude reaction product was allowed to melt and transferred to 2 mL centrifuge tubes for purification. The mixture was centrifuged for 10 minutes at 7,000 rpm and the precipitate was dispersed in 2.4 mL of toluene. To remove excess ligands, 8.2 mL of ethyl acetate was added and the mixture was again centrifuged for 10 minutes at 7,000 rpm. The precipitate was collected, dispersed in a mixture of 1.2 mL of toluene and 8.2 mL of ethyl acetate and was then centrifuged for 10 minutes at 7,000 rpm. The precipitate was subsequently collected and dispersed in 0.8 mL of hexane and centrifuged for 5 minutes at 4,400 rpm to remove aggregates. Finally, the supernatant was collected and centrifuged for 8 minutes at 12,000 rpm to remove large nanoparticles.

4 (or 6) layer thick Nanoplates

Cesium carbonate (24.32 mg, 0.074 mmol), lead acetate trihydrate (114 mg, 0.3 mmol) and ODE (7.5 mL, 23.4 mmol) were loaded into a 20 mL vial and dried under vacuum for 1h at 120 °C. To this suspension, dry OA (0.98 ml, 3.0 mmol) and OLAm (0.95 ml, 3.0 mmol) were added under an inert atmosphere and precursors were allowed to dissolve with stirring for 30 minutes. The temperature was then lowered to 75 °C (85 °C for 6 layers thick nanoplates) and allowed to stabilize for 10 minutes. Benzoyl bromide (0.11 mL, 0.9 mmol) was added quickly and the reaction mixture was immediately cooled down in an ice-water bath.

The crude reaction product was allowed to melt and transferred to 2 mL centrifuge tubes for purification. The mixture was centrifuged for 10 minutes at 7,000 rpm and the precipitate was dispersed in 2.4 mL of toluene. To remove excess ligands, 8.2 mL of ethyl acetate was added and the mixture was again centrifuged for 10 minutes at 7,000 rpm. The precipitate was collected, dispersed in a mixture of 1.2 mL of toluene and 8.2 mL of ethyl acetate and was then centrifuged for 10 minutes at 7,000 rpm. The precipitate was subsequently collected and dispersed in 0.8 mL of toluene and centrifuged for 5 minutes at 4,400 rpm to remove aggregates. Finally, the supernatant was collected and centrifuged for 8 minutes at 12,000 rpm to remove large nanoparticles.

Characterization.

Ultraviolet and visible absorption (UV-vis) spectra for colloidal solutions were taken using a Cary 5000 UV-vis-NIR spectrophotometer. AFM images and size distribution data were acquired from a Nanoscope Dimension CSPM5500 atomic force microscope under the tapping mode. For the sample preparation, films of nanoplates were spun cast (1,500 RPM from toluene) onto clean silicon wafers coated with a thin film of polymerized methane used to prevent aggregation.[15] Measurements were background corrected before extracting the NPL height. Photoluminescence measurements were recorded using a NanoLog spectrofluorometer. TEM images and data were taken from a FEI Tecnai G220 S-TWIN electron microscope operating at 200 kV with a Gatan SC200 CCD camera. PXRD data were acquired using a Bruker AXS D8 Discover GADDS X-Ray Diffractometer equipped with a Vantec-500 area detector and is operated at 35 kV and 40 mA at a wavelength of Co $K\alpha$ (1.79 Å). The calculated XRD pattern was

determined using the Vesta software package (input cobalt x-ray source wavelengths Cu-$K\alpha_1$ = 1.54059 Å and Cu-$K\alpha_2$ = 1.54432 Å, with a relative intensity of 1 and 0.5 respectively). SEM images were taken from a Zeiss Gemini Ultra-55 analytical field emission scanning electron microscope.

ASSOCIATED CONTENT

Supporting Information.

The Supporting Information is available free of charge online.

AUTHOR INFORMATION

Corresponding Author

*E-mail (Carolin Sutter-Fella): csutterfella@lbl.gov

*E-mail (Yi Liu): yliu@lbl.gov

*E-mail (Matthew Jurow): MJurow@lbl.gov

Notes

The authors declare no competing financial interest.

Author Contributions

Y.L., M.J.J., and C.M.S.-F. initiated this research. M.D. developed the synthesis. M.D. and I.K. conducted the synthesis and in situ experiments. M.A.K. and G.K. did AFM and TEM measurements and analysis. J.K. and L.-W.W. did DFT calculations. M.D., N.S.B., and Z.Y. wrote codes to evaluate the data. M.D., I.K., Y.L., M.J.J. and C.M.S.-F. evaluated the data. The manuscript was written by M.D., I.K., M.J.J. and C.M.S.-F. All authors have given approval to the final version of the manuscript.

Acknowledgements

This manuscript was prepared with support from the Laboratory Directed Research and Development (LDRD) program of Lawrence Berkeley National Laboratory under U.S. Department of Energy contract number DE-AC02-05CH11231 (C.M.S.-F.). This work was supported by the U.S. Department of Energy, Office of Science, Office of Basic Energy Sciences, Materials Sciences and Engineering Division, under Contract No. DE-AC02-05CH11231 within the Inorganic/Organic Nanocomposites Program (KC3104). Work at the Molecular Foundry was supported by the Office of Science, Office of Basic Energy Sciences, of the U.S. Department of Energy under Contract No. DE-AC02-05CH11231 (M.J.J, Y.L.). This work was supported in part by the U.S. Department of Energy, Office of Science, Office of Workforce Development for Teachers and Scientists (WDTS) under the Science Undergraduate Laboratory Internships Program (SULI) (M.D.). We highly appreciate support with coding provided by Thi Mach.

References

1. Q. A. Akkerman, S. G. Motti, A. R. Srimath Kandada, E. Mosconi, V. D'Innocenzo, G. Bertoni, S. Marras, B. A. Kamino, L. Miranda, F. De Angelis, A. Petrozza, M. Prato and L. Manna, *Journal of the American Chemical Society*, 2016, **138**, 1010-1016.
2. Y. Bekenstein, B. A. Koscher, S. W. Eaton, P. Yang and A. P. Alivisatos, *Journal of the American Chemical Society*, 2015, **137**, 16008-16011.
3. M. C. Brennan, J. Zinna and M. Kuno, *ACS Energy Letters*, 2017, **2**, 1487-1488.
4. A. Pan, B. He, X. Fan, Z. Liu, J. J. Urban, A. P. Alivisatos, L. He and Y. Liu, *ACS Nano*, 2016, **10**, 7943-7954.
5. S. Sun, D. Yuan, Y. Xu, A. Wang and Z. Deng, *ACS Nano*, 2016, **10**, 3648-3657.
6. A. K. Geim and K. S. Novoselov, *Nature Materials*, 2007, **6**, 183.
7. H. Huang, L. Polavarapu, J. A. Sichert, A. S. Susha, A. S. Urban and A. L. Rogach, *Npg Asia Materials*, 2016, **8**, e328.
8. X. Huang, S. Tang, X. Mu, Y. Dai, G. Chen, Z. Zhou, F. Ruan, Z. Yang and N. Zheng, *Nature Nanotechnology*, 2010, **6**, 28.
9. Y. Lin, T. V. Williams and J. W. Connell, *The Journal of Physical Chemistry Letters*, 2010, **1**, 277-283.
10. K. S. Novoselov, A. K. Geim, S. V. Morozov, D. Jiang, Y. Zhang, S. V. Dubonos, I. V. Grigorieva and A. A. Firsov, *Science*, 2004, **306**, 666.
11. C. Tan, X. Qi, X. Huang, J. Yang, B. Zheng, Z. An, R. Chen, J. Wei, B. Z. Tang, W. Huang and H. Zhang, *Advanced Materials*, 2013, **26**, 1735-1739.
12. W. Zheng, P. Huang, Z. Gong, D. Tu, J. Xu, Q. Zou, R. Li, W. You, J.-C. G. Bünzli and X. Chen, *Nature Communications*, 2018, **9**, 3462.
13. M. V. Kovalenko, L. Protesescu and M. I. Bodnarchuk, 2017, **358**, 745-750.
14. L. Protesescu, S. Yakunin, M. I. Bodnarchuk, F. Krieg, R. Caputo, C. H. Hendon, R. X. Yang, A. Walsh and M. V. Kovalenko, *Nano Letters*, 2015, **15**, 3692-3696.
15. M. J. Jurow, T. Lampe, E. Penzo, J. Kang, M. A. Koc, T. Zechel, Z. Nett, M. Brady, L.-W. Wang, A. P. Alivisatos, S. Cabrini, W. Brütting and Y. Liu, *Nano Letters*, 2017, **17**, 4534-4540.
16. Y. Dong, T. Qiao, D. Kim, D. Parobek, D. Rossi and D. H. Son, *Nano Letters*, 2018, **18**, 3716-3722.
17. A. Dutta, S. K. Dutta, S. Das Adhikari and N. Pradhan, *ACS Energy Letters*, 2018, **3**, 329-334.
18. M. Imran, V. Caligiuri, M. Wang, L. Goldoni, M. Prato, R. Krahne, L. De Trizio and L. Manna, *Journal of the American Chemical Society*, 2018, **140**, 2656-2664.
19. J. Shamsi, Z. Dang, P. Bianchini, C. Canale, F. Di Stasio, R. Brescia, M. Prato and L. Manna, *Journal of the American Chemical Society*, 2016, **138**, 7240-7243.
20. S. A. Veldhuis, P. P. Boix, N. Yantara, M. Li, T. C. Sum, N. Mathews and S. G. Mhaisalkar, *Adv. Mater.*, 2016, **28**, 6804-6834.
21. B. R. Sutherland and E. H. Sargent, *Nat Photon*, 2016, **10**, 295-302.
22. G. Hodes, *Science*, 2013, **342**, 317-318.
23. J. S. Manser, J. A. Christians and P. V. Kamat, *Chem. Rev. (Washington, DC, U. S.)*, 2016, **116**, 12956-13008.
24. S. Colella, M. Mazzeo, A. Rizzo, G. Gigli and A. Listorti, *The Journal of Physical Chemistry Letters*, 2016, **7**, 4322-4334.

25. L. A. Bauer, N. S. Birenbaum and G. J. Meyer, *Journal of Materials Chemistry*, 2004, **14**, 517-526.
26. R. M. Fratila, S. Rivera-Fernández and J. M. de la Fuente, *Nanoscale*, 2015, **7**, 8233-8260.
27. R. Sahay, P. Suresh Kumar, V. Aravindan, J. Sundaramurthy, W. Chui Ling, S. G. Mhaisalkar, S. Ramakrishna and S. Madhavi, *The Journal of Physical Chemistry C*, 2012, **116**, 18087-18092.
28. Y. Tang, Y. Zhang, J. Deng, D. Qi, W. R. Leow, J. Wei, S. Yin, Z. Dong, R. Yazami, Z. Chen and X. Chen, 2014, **53**, 13488-13492.
29. Y. Liu, G. Zhou, K. Liu and Y. Cui, *Accounts of Chemical Research*, 2017, **50**, 2895-2905.
30. C. E. Rowland, I. Fedin, H. Zhang, S. K. Gray, A. O. Govorov, D. V. Talapin and R. D. Schaller, *Nature Materials*, 2015, **14**, 484.
31. D. Yang, Y. Zou, P. Li, Q. Liu, L. Wu, H. Hu, Y. Xu, B. Sun, Q. Zhang and S.-T. Lee, *Nano Energy*, 2018, **47**, 235-242.
32. J. C. Ford, *Journal of the American Chemical Society*, 1997, **119**, 5079-5079.
33. J. De Roo, M. Ibáñez, P. Geiregat, G. Nedelcu, W. Walravens, J. Maes, J. C. Martins, I. Van Driessche, M. V. Kovalenko and Z. Hens, *ACS Nano*, 2016, **10**, 2071-2081.
34. V. A. Hintermayr, A. F. Richter, F. Ehrat, M. Döblinger, W. Vanderlinden, J. A. Sichert, Y. Tong, L. Polavarapu, J. Feldmann and A. S. Urban, *Advanced Materials*, 2016, **28**, 9478-9485.
35. C. Schliehe, B. H. Juarez, M. Pelletier, S. Jander, D. Greshnykh, M. Nagel, A. Meyer, S. Foerster, A. Kornowski, C. Klinke and H. Weller, *Science*, 2010, **329**, 550.
36. A. Jain, S. P. Ong, G. Hautier, W. Chen, W. D. Richards, S. Dacek, S. Cholia, D. Gunter, D. Skinner, G. Ceder and K. Persson, *APL Materials*, 2013, **1**, 011002.
37. H.-X. Deng, S.-S. Li and J. Li, *The Journal of Physical Chemistry C*, 2010, **114**, 4841-4845.
38. J. L. Rodgers and W. A. Nicewander, *The American Statistician*, 1988, **42**, 59-66.
39. B. Luo, Y.-C. Pu, S. A. Lindley, Y. Yang, L. Lu, Y. Li, X. Li and J. Z. Zhang, 2016, **55**, 8864-8868.
40. B. Luo, S. B. Naghadeh, A. L. Allen, X. Li and J. Z. Zhang, 2017, **27**, 1604018.
41. G. Almeida, L. Goldoni, Q. Akkerman, Z. Dang, A. H. Khan, S. Marras, I. Moreels and L. Manna, *ACS Nano*, 2018, **12**, 1704-1711.
42. G. Kresse and J. Furthmüller, *Physical Review B*, 1996, **54**, 11169-11186.
43. G. Kresse and D. Joubert, *Physical Review B*, 1999, **59**, 1758-1775.
44. J. P. Perdew, K. Burke and M. Ernzerhof, *Phys. Rev. Lett.*, 1997, **78**, 1396-1396.

ToC

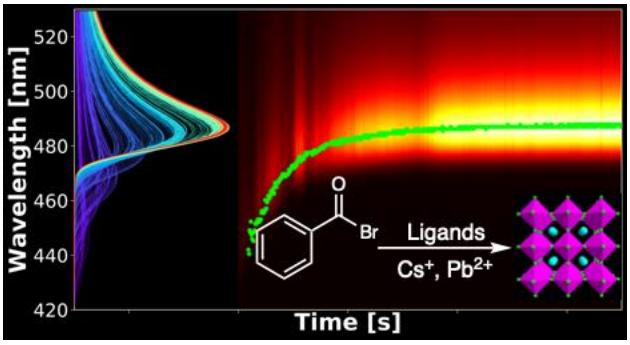
Wavelength [nm]
520
500
480
460
440
420
Time [s]
O
Br
Ligands
Cs+, Pb2+